processes

MDPI

Article

An Analysis of the Vacuum Generation Mechanism and Prototype Study of Negative-Pressure Suction-Type Cuttings Reduction Equipment

Xin Wang *, Bo Zhang, Zhuo Wang and Hongwen Ma

School of Mechanical and Electrical Engineering, Harbin Engineering University, Harbin 150001, China
* Correspondence: wangxin666@hrbeu.edu.cn

Abstract

In the context of increasingly complex offshore drilling operations and stricter environmental regulations, the efficient handling and volume reduction of drilling cuttings has emerged as a crucial focus in the advancement of solids control equipment. "Airflow-assisted screening" is a technique that uses directed air currents to enhance the separation of solid cuttings from drilling fluid on a shaker screen, thereby improving dewatering efficiency and reducing waste volume during drilling. This study proposes and designs novel negative-pressure suction-type cuttings reduction equipment by integrating this technology with screw conveying principles. The system features a compact, vacuum-generator-centered design that integrates suction and screening. Key components were optimized, and a monitoring scheme was implemented for real-time performance evaluation. In the mechanism analysis, the relationship between inlet pressure, geometric parameters, and suction performance was explored based on Bernoulli's principle and Laval nozzle characteristics, and internal flow field characteristics were revealed through computational fluid dynamics (CFDs) simulations. In the experimental section, a prototype system and testing platform were constructed to evaluate the effects of inlet pressure and screen mesh configurations on suction and screening performance. The results indicate that the system achieved optimal performance at an inlet pressure of 400 kPa with a 100-mesh screen, reaching a cuttings reduction efficiency of 9.225%. This study effectively validates the theoretical and simulation findings, providing technical support for the application of this equipment in complex drilling environments and demonstrating strong potential for practical implementation.

Keywords: cuttings reduction; negative-pressure suction; vacuum generator; prototype experiment

Check for updates

Academic Editor: Massimo Caruso

Received: 6 December 2025
Revised: 6 February 2026
Accepted: 6 February 2026
Published: 10 February 2026

Copyright: © 2026 by the authors. Licensee MDPI, Basel, Switzerland. This article is an open access article distributed under the terms and conditions of the Creative Commons Attribution (CC BY) license.

1. Introduction

With growing energy demand in China, offshore oil and gas exploration and development have accelerated, making nearshore regions, such as the Bohai Sea and the South China Sea, important strategic areas [1]. During offshore drilling operations, drill cuttings—as the primary solid waste—often carry a significant amount of drilling fluid. Without effective treatment, this not only results in material waste but also risks polluting the marine environment due to oil content and heavy metals [2,3]. This issue is particularly prominent in Class I marine areas like the Bohai Sea, where strict environmental regulations impose stringent requirements on waste discharge [4]. The traditional practice of transporting waste back to land for processing is costly and risky, making efficient on-site

 https://doi.org/10.3390/pr14040618

waste reduction on offshore platforms an increasingly urgent need [5]. Although current solids control equipment, such as shale shakers and centrifuges, is relatively mature, it is primarily designed for oil-based drilling fluids. When dealing with high-liquid-content mixtures from water-based drilling fluids, their dewatering and reduction capabilities remain insufficient [6]. Water-based drilling fluids, favored for their environmental compatibility and cost-effectiveness [7], present challenges in solid–liquid separation. Existing equipment requires urgent improvements in continuity and processing efficiency, highlighting the need for innovation in both technology and design concepts [8]. Rational configuration of solids control equipment and the development of an efficient drilling fluid solids control system are key to promptly removing harmful solid particles, stabilizing fluid properties, and ensuring fluid reusability. Studies indicate that the current application of negative-pressure suction technology in offshore oilfield solids control systems is mainly concentrated in the shale shaker stage [9,10]. In 2004, Norway's Cubility (Sandnes, Norway) proposed the MudCube solids control system, aiming to automatically suction, separate, and transport drill cuttings in an enclosed environment [11]. In 2015, the U.S.-based M-I SWACO company (Houston, TX 77072, USA) developed the SCREEN PULSE™ system, which introduced pulse back-blow technology to shale shakers, simultaneously enhancing drilling fluid recovery and cuttings drying [12]. In 2018, Zhou Sizhu's team at Yangtze University designed a novel negative-pressure drilling shaker with a vacuum chamber beneath the screen surface to enhance screening efficiency and fluid handling capacity through a pressure differential [13]. Between 2019 and 2023, Ma Weiguo and others studied a solid–liquid separation device that integrates vacuum belt filtration with micro-vibration, using a combined mesh-belt structure [14,15]. The vacuum generator originates from a unidirectional gas–gas ejector device [16], which creates negative pressure through specific structural design, drawing heavily from ejector theory and simulation methods. In 1960, Soviet scientist Sokolov systematically explained the design and calculation of ejectors in his book *Ejectors*, introducing the concept of gas dynamic functions and providing theoretical calculations for various types of ejectors [17], laying the foundation for future research. In 2016, Canadian scholar Croquer et al. conducted comparative simulations of the Standard *k*–ε and SST *k*–ω models in predicting gas ejector performance and found that the SST *k*–ω model better captured shock wave structures [18]. That same year, Li Tianmin, from China's University of Petroleum, combined theory, simulation, and experiments to study the working characteristics of jet vacuum pumps, analyzing how structural parameters and new nozzle designs affect performance [19]. In 2020, Professor Dong Jingming, from Dalian Maritime University, conducted 3D numerical simulations of ejector flow fields, investigating how jet parameters vary with time under different cross-section lengths, Mach numbers, and mixing chamber lengths [20]. In 2021, Professor Wang Zhongyi and colleagues, from Qingdao University of Science and Technology, conducted numerical simulations to analyze the influence of inlet pressure and outlet backpressure on vacuum levels in vacuum generators during negative-pressure conveyance [21]. In 2023, Wang Zhiwen et al., from Dalian Maritime University, proposed a novel algorithm through numerical simulation. This method quantifies energy losses and their spatiotemporal distribution within vacuum generators, offering new perspectives for their analysis, evaluation, design, and optimization [22]. In 2024, Professor Yang Jianmin and colleagues at Shanghai Jiao Tong University analyzed the flow field characteristics of coupled collection, swirl collection, and negative-pressure suction flow collection, along with the roles of various power sources during the ore collection process [23]. This paper first proposes a novel design for a negative-pressure suction-type cuttings reduction device, incorporating a shaftless screw conveyor and optimizing key parameters, such as airflow rate and pipe diameter, to enhance system stability and operational efficiency. Then, it analyzes the working principle

of the vacuum generator, which generates negative pressure through a Laval nozzle, with optimizations in vacuum level and suction flow rate.

The existing literature demonstrates significant progress in applying negative pressure to cuttings separation, yet several challenges remain:

(1) Most systems are batch-operated rather than continuous;
(2) Vacuum stability is compromised when handling high-moisture cuttings;
(3) Real-time performance monitoring is rarely integrated.

In contrast to existing negative-pressure systems primarily applied to shale shakers, this study integrates a shaftless screw conveyor with a multi-stage vacuum suction system, enabling continuous, in situ separation of high-liquid-content cuttings. The novelty lies in the synergistic combination of pneumatic conveyance, real-time weight monitoring, and optimized Laval nozzle geometry for enhanced vacuum stability and separation efficiency. Finally, a prototype was built for performance testing.

2. The Design of a Negative-Pressure Suction-Based Cuttings Reduction System

This section focuses on the overall design of the negative-pressure suction-based cuttings reduction equipment, proposing a design scheme and emphasizing the structure of the vacuum suction device, the pneumatic transmission circuit, and the control circuit design. It also analyzes key parameter calculation methods. Additionally, an airflow monitoring and weight detection system is designed to ensure the equipment's stability and intelligence. These studies lay the foundation for subsequent analysis of the vacuum mechanism and the cuttings screening behavior.

2.1. Overall Design Scheme of Negative-Pressure Suction-Based Cuttings Reduction Equipment

This paper proposes a negative-pressure spiral separation device (see Figure 1) that uses a vacuum suction section on the screw conveyor and secondary liquid removal by a vacuum pump to reduce cuttings moisture and improve processing efficiency.

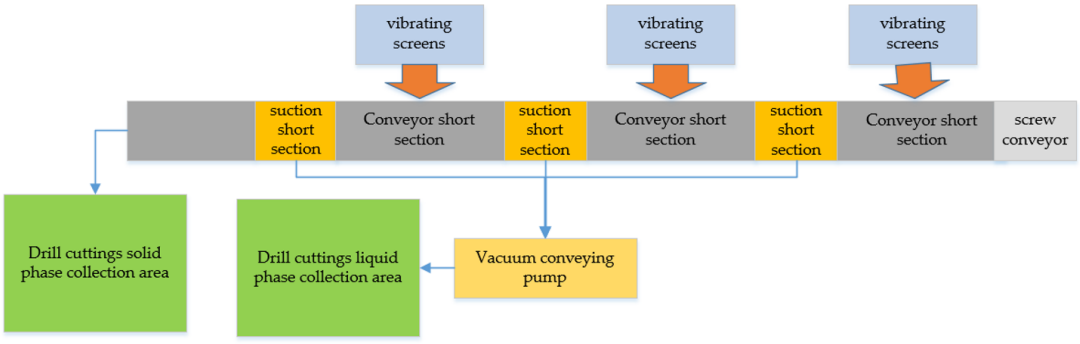


Figure 1. A layout diagram of the negative-pressure spiral separation and reduction device.

This paper presents a design for a negative-pressure spiral separation and reduction device (see Figure 2), in which three vacuum suction sections are connected to a vacuum transfer pump to form a suction system that works in conjunction with a screw conveyor. The device generates negative pressure using an external air source and the Venturi principle, enabling liquid phase separation from drill cuttings and remote discharge. Its core components include a vacuum generator, storage tank, and pneumatic control system to ensure efficient operation. Equipped with six suction sections, each independently controlling liquid separation, the device ultimately discharges the reduced cuttings into the solid-phase collection zone.

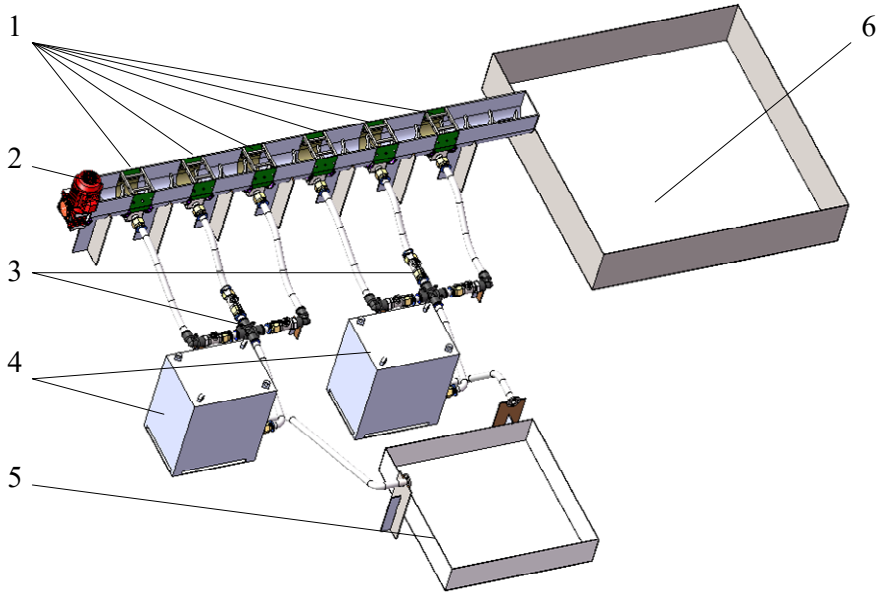


Figure 2. The overall structure of the negative-pressure spiral separation and reduction device. 1—negative-pressure suction section; 2—screw conveyor; 3—transfer pipeline; 4—vacuum transfer pump; 5—drill cuttings liquid collection area; and 6—drill cuttings solid collection area.

2.2. The Design of the Vacuum Suction Unit

The negative-pressure suction section recovers the liquid phase from drill cuttings by creating a vacuum, coordinating the cuttings transport and liquid suction flow to reduce moisture content. Its structure, shown in Figure 3, mainly consists of a working beam, outer shell, liner clamp, filtration module, connecting ribs, support ribs, and a vacuum chamber. The filtration module separates solids from liquids, with the liquid phase delivered through pipelines to the recovery system, thereby improving processing efficiency.

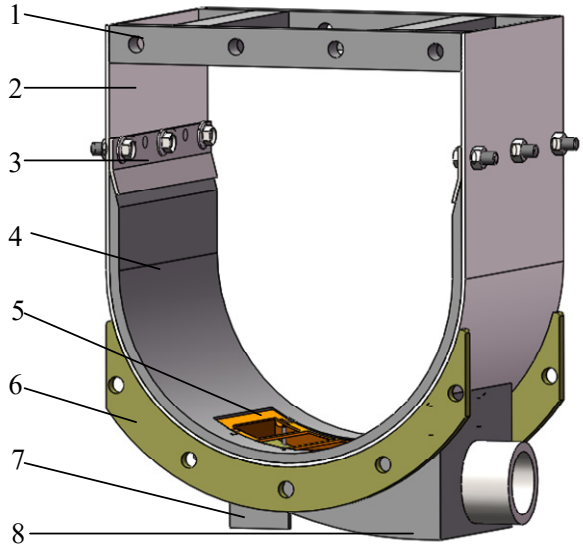


Figure 3. The structure of the negative-pressure suction section. 1—working beam; 2—outer shell; 3—liner clamp; 4—liner; 5—filtration module; 6—connecting rib; 7—support rib; and 8—vacuum chamber.

The filtration module, as shown in Figure 4, mainly consists of a top cover plate, middle support, bottom support plate, and a wire mesh screen.

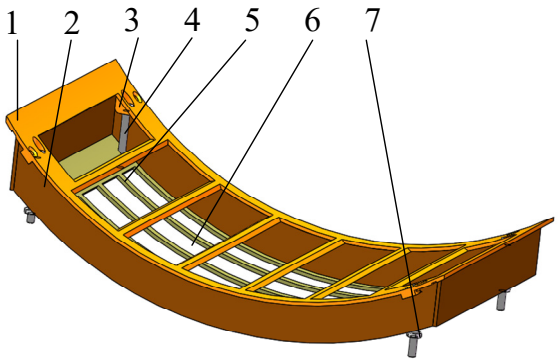


Figure 4. The filtration module of the negative-pressure suction section. 1—top cover plate; 2—middle support; 3—top cover boss; 4—adjustment bolt; 5—bottom support plate; 6—mesh placement area; and 7—adjustment nut.

In the vacuum suction system, the transfer pipeline connects the negative-pressure suction sections to the vacuum pump and is responsible for transporting the liquid phase material. A circular pipe structure is adopted to ensure uniform mixing. Pressure loss in the pipeline system is a major source of energy consumption, and the layout, dimensions, and material selection of the pipes significantly affect system performance.

The vacuum transfer pump operates by using a vacuum generation component to create negative pressure in the storage tank, thereby enabling efficient material suction through the feed pipe. The design scheme is shown in Figure 5.

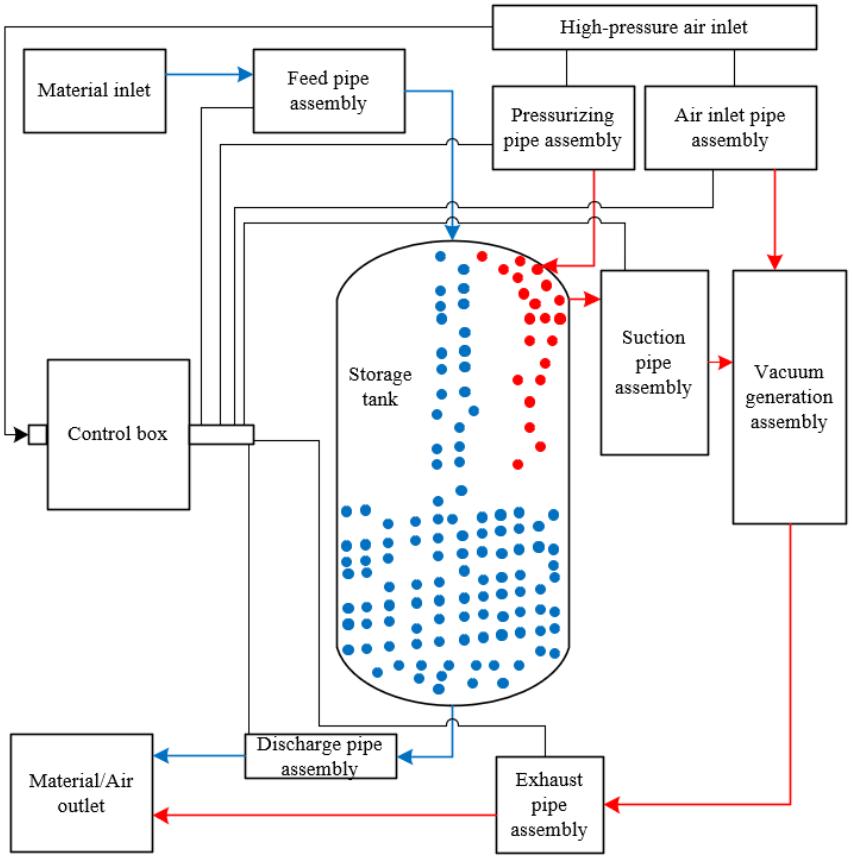


Figure 5. The design scheme of the vacuum transfer pump.

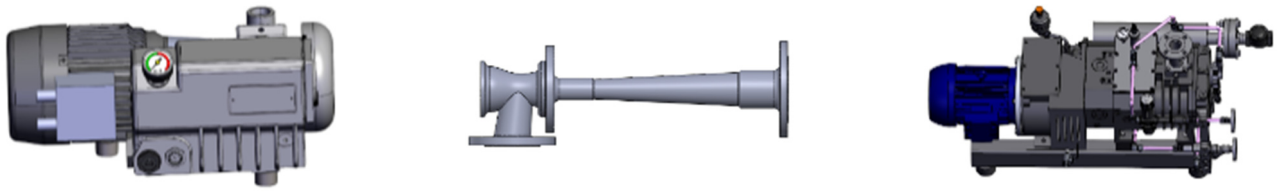
The working principle of the vacuum transfer pump is as follows:

a. Material suction: High-pressure gas enters the vacuum generation unit through the air intake pipe, creating negative pressure at the suction pipe inlet. Air mixes with

compressed gas and is discharged, forming a vacuum inside the tank. Driven by atmospheric pressure, the material is drawn through the negative-pressure suction sections and the transfer pipeline into the storage tank.

b. Material discharge: After suction is complete, compressed gas stops entering the vacuum generation unit and instead enters the storage tank through the pressurizing pipe assembly, increasing the tank pressure. The material is expelled by the high-pressure gas, and the feed pipe assembly backflushes the filter screen.

In the vacuum suction system, the vacuum generation device is the key component determining overall performance. Its influencing factors include vacuum level, airflow, transport efficiency, and energy consumption. For this study, selecting an appropriate vacuum generation unit was crucial for improving system efficiency and reducing energy consumption. Currently, common vacuum generation methods mainly involve vacuum pumps. According to their working principles, vacuum pumps can be classified into mechanical pumps (using compression and suction), jet pumps (using high-speed working fluids), and capture pumps (using condensation, adsorption, or reaction), each suitable for different vacuum levels and application scenarios, as shown in Figure 6.



(**a**) Mechanical-Type (**b**) Jet-Type (**c**) Capture-Type

Figure 6. Types of vacuum pumps.

To meet the requirements of limited space and high flow suction on offshore drilling platforms, this study selected a jet-type vacuum pump (hereinafter referred to as the vacuum generator) as the vacuum source, leveraging the stable compressed air resources on-site to achieve efficient and energy-saving suction operations.

2.3. Design Rationale and Parameter Optimization

The selection of key design parameters was guided by both theoretical analysis and practical constraints. The six suction sections were determined through preliminary CFD simulations to ensure uniform pressure distribution along the 2.5 m conveyor length. The pipeline inner diameter of 65 mm was optimized using the Darcy–Weisbach equation to minimize pressure loss while maintaining structural feasibility. The 100-mesh stainless steel screen (aperture = 0.15 mm) was selected after comparative trials with 50, 100, 140, and 200 mesh screens, balancing separation efficiency (capturing fine particles) with resistance to clogging—a critical consideration for continuous operation. The fill rate of 15–30% was chosen based on preliminary tests to prevent overloading while maintaining adequate material flow for effective suction.

3. Analysis of the Vacuum Generation Mechanism in the Vacuum Suction Device

This section first analyzes the fundamental principle of vacuum generation by fluid flow based on Bernoulli's equation and explores the influence of inlet parameters on vacuum level and suction flow rate. Subsequently, an in-depth study of the vacuum generator's working mechanism is conducted, focusing on its internal fluid dynamics characteristics, including the Laval tube effect, entrainment coefficient, and geometric parameters.

3.1. Analysis of Vacuum Generation Principle Based on Bernoulli's Equation

3.1.1. Analysis of Vacuum vs. Fluid Input Parameters

The initial analysis based on Bernoulli's equation assumes steady, incompressible, inviscid flow to establish fundamental relationships between pressure and velocity. These assumptions are valid for low-speed (Ma < 0.3) flow regions typical of the suction piping; for high-speed compressible flow in the Laval nozzle section, corrections based on compressible flow theory are applied in Section 3.2 [24]. As illustrated in Figure 7, the fluid flowing from a wide cross-section (A_2) to a narrow cross-section (A_2) satisfies the relationship given in Equation (1).

$$\frac{p_2}{\rho_2} + \frac{1}{2}v_2^2 + gh_2 = \frac{p_1}{\rho_1} + \frac{1}{2}v_1^2 + gh_1 \quad (1)$$

where p_1—the absolute pressure at the converging section, Pa;

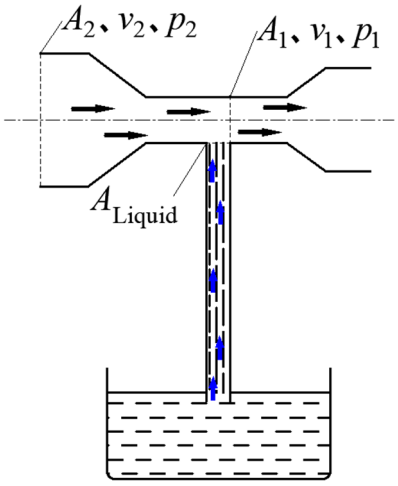


Figure 7. Schematic diagram of Bernoulli's equation analysis.

p_2—the absolute pressure at the inlet, Pa;
ρ_1—the fluid density at the converging section, kg/m^3,
ρ_2—the fluid density at the Inlet, kg/m^3;
v_1—the fluid velocity at the converging section, m/s;
v_2—the fluid velocity at the inlet, m/s;
g—the gravitational acceleration, 9.81 m/s^2;
h—the height, m.

In pneumatic components, the elevation term (gh) is often neglected because it is much smaller than the kinetic energy term, and the fluid is assumed incompressible, i.e., ($\rho_1 = \rho_2 = \rho$). Combined with the continuity equation ($A_2v_2 = A_1v_1$) and the fluid flow rate inside the pipe ($Q_{im} = A_2v_2$), the vacuum degree at the converging section can thus be obtained as:

$$p_{vac} = p_{atm} - p_1 = p_{atm} - p_2 + \frac{1}{2}\rho\frac{Q_{im}^2}{A_2^2}\left(\frac{A_2^2}{A_1^2} - 1\right) \quad (2)$$

where p_{vac}—vacuum degree, Pa; p_{atm}—atmospheric pressure, Pa; ρ—fluid density, kg/m^3; and Q_{im}—input fluid flow rate, m^3/s.

Keeping the overall structure fixed, i.e., with A_2/A_1 as a constant, the input fluid is selected as liquid water, and the input liquid pressure is set to four different values. Using Equation (2) and visualization through analysis software, the results are shown in Figure 8.

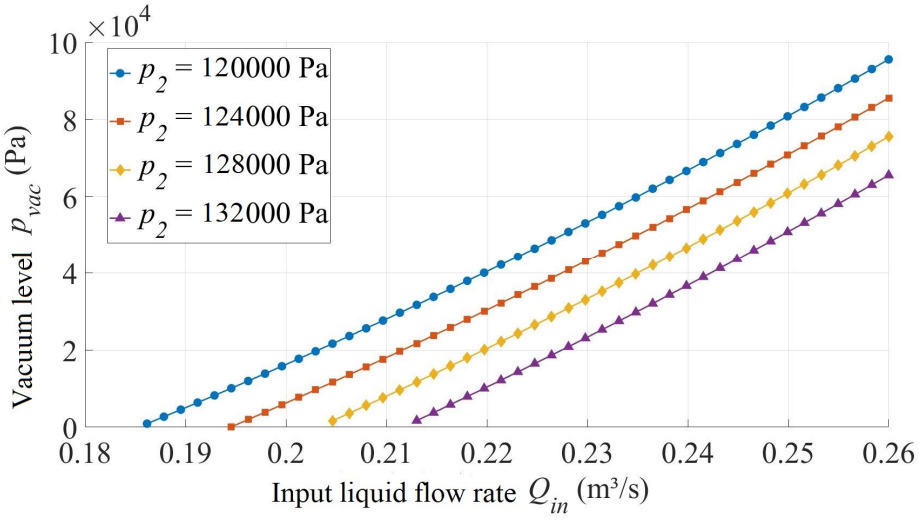


Figure 8. Variation in inlet liquid flow rate and vacuum degree under different inlet pressures.

The analysis indicates that the liquid flow rate within the tube exhibits a quadratic relationship with the vacuum degree. Furthermore, an increase in inlet gas flow rate leads to an increase in vacuum degree, whereas a higher inlet liquid pressure results in a decreasing trend in vacuum degree.

3.1.2. Analysis of the Correlation Between the Suction Liquid Flow Rate and Input Fluid Parameters

As illustrated in Figure 7, liquid (assumed to be water) flows from the top of the storage tank—initially at rest—toward the upper suction inlet. The initial velocity is considered zero, with atmospheric pressure p_{atm} at the tank top and pressure p_1 at the suction inlet. By applying Bernoulli's equation to the vertical suction pipe and neglecting viscous losses, the following expression is obtained:

$$Q_{suc} = A_{suc} \cdot \sqrt{2\left(\frac{P_{atm} - P_2}{\rho} - gh\right) + \left(\frac{Q_{im}}{A_2}\right)^2 \left(\frac{A_2^2}{A_1^2} - 1\right)} \tag{3}$$

where A_{suc} is the suction port cross-sectional area (m^2).

According to Equation (3), and utilizing analysis software for visualization, the system is considered to have a fixed structure, where A_1/A_2 and A_{Liquid} are constant. The inlet gas pressure is varied across four different values, as illustrated in Figure 9.

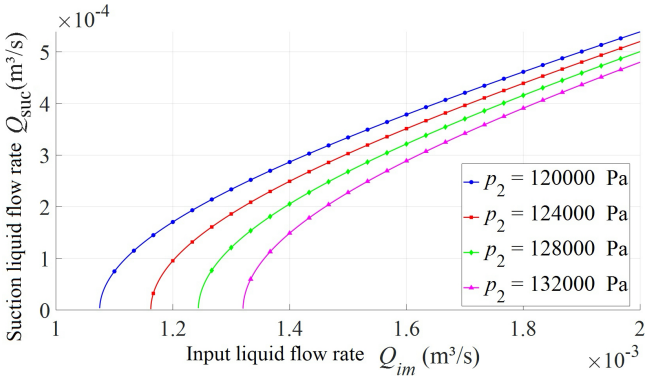


Figure 9. Variation of suction liquid flow rate with inlet liquid flow rate under varying inlet liquid pressures.

The analysis reveals that the suction liquid flow rate is positively correlated with the inlet liquid flow rate and negatively correlated with the inlet gas pressure. In addition,

Figure 9 demonstrates the existence of a minimum threshold for the inlet liquid flow rate, below which effective liquid suction cannot be achieved.

3.2. Vacuum Generator: Mechanism and Performance Analysis

Section 3.2 provides a preliminary conclusion that the static pressure decreases as the fluid passes through the narrow section of the nozzle at high velocity, resulting in negative pressure at the suction port. This phenomenon can be explained by Bernoulli's equation. However, when the gas velocity approaches or exceeds the speed of sound, notable variations in density necessitate corrections based on compressible flow theory. The following discussion will delve deeper into the working mechanism of the vacuum generator and the associated fluid dynamic processes.

3.2.1. Hydrodynamic Analysis of the Laval Nozzle

The relationships presented in Equation (4) are derived by applying the differential forms of the one-dimensional steady flow continuity and momentum equations, in conjunction with the gas state equation.

$$\begin{aligned} \frac{dv}{v} &= \frac{1}{Ma^2-1}\frac{dA}{A};\ \frac{d\rho}{\rho} = \frac{-Ma^2}{Ma^2-1}\frac{dA}{A} \\ \frac{dT}{T} &= \frac{-(\kappa-1)Ma^2}{Ma^2-1}\frac{dA}{A};\ \frac{dp}{p} = \frac{-\kappa Ma^2}{Ma^2-1}\frac{dA}{A} \end{aligned} \tag{4}$$

where Ma—the Mach number of the gas;

A—the cross-sectional area at an arbitrary location in the Laval nozzle, m^2;

T—the thermodynamic temperature at an arbitrary location in the Laval nozzle, K;

p—the pressure at an arbitrary location in the Laval nozzle, Pa;

v—the gas flow velocity at an arbitrary location in the Laval nozzle, m/s;

ρ—the gas density at an arbitrary location in the Laval nozzle, kg/m^3;

κ—the isentropic index, which can be assumed as 1.4.

Visualization based on the system of Equation (4) yields curves illustrating the effect of cross-sectional area variation along the flow tube on airflow parameters across different Mach number ranges, as presented in Figure 10.

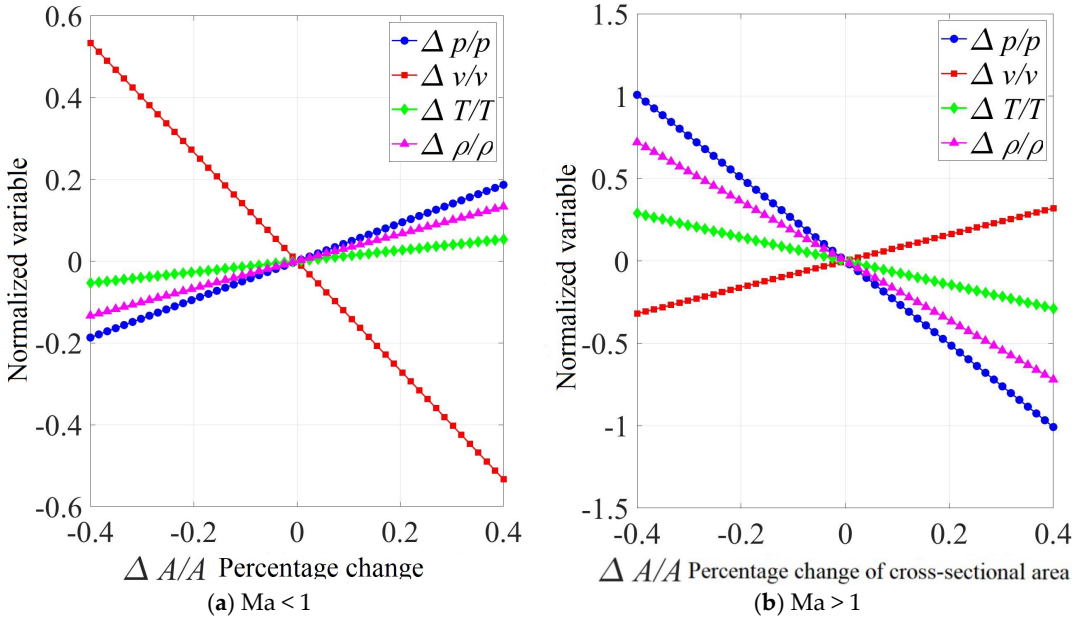


Figure 10. Impact of cross-sectional area changes on airflow parameters across various Mach number regimes.

From the curves, the influence of pipe cross-sectional area changes on different airflow parameters is summarized in Table 1.

Table 1. A summary of the influence of pipe cross-sectional area changes on airflow parameters under different Mach number regimes, derived from the theoretical analysis of Equation (4) and the trends illustrated in Figure 10.

Flow Region	Geometric Conditions	Conclusion
subsonic flow $Ma < 1$	converging tube A decreases	v, Ma enlarge ρ, p, T decrease
	diverging tube A enlarge	v, Ma decrease ρ, p, T enlarge
supersonic flow $Ma > 1$	converging tube A decreases	v, Ma decrease ρ, p, T enlarge
	diverging tube A enlarge	v, Ma enlarge ρ, p, T decrease
sonic flow $Ma = 1$	constant cross-section A constant	all parameters remain constant

In summary, increasing the gas velocity leads to a decrease in static pressure, and when the velocity reaches a certain threshold, negative pressure is formed, resulting in vacuum generation. The Laval nozzle leverages this principle through its variable cross-section design—first converging, then diverging—which accelerates the gas flow to supersonic speeds within the nozzle, thereby improving the vacuum level of the vacuum generator.

3.2.2. The Ejector Coefficient and Geometric Parameter Analysis of the Vacuum Generator

Based on Figure 11, the momentum equation is applied to analyze the gas within the mixing chamber, which includes the converging section and the cylindrical section, resulting in Equation (5):

$$\begin{aligned} &\varphi_2(q_{mP}v_{P2} + q_{mH}v_{H2}) - (q_{mP} + q_{mH})v_3 = \\ &p_3A_3 + \int_{A_2}^{A_3} pdA - p_{P2}A_{P2} - p_{H2}A_{H2} \end{aligned} \tag{5}$$

where q_m—mass flow rate (kg/s);

v_P, v_H—velocities of primary (driving) fluid and secondary (suction) fluid (m/s);

p_P, p_H—pressures of primary and secondary fluids (Pa).

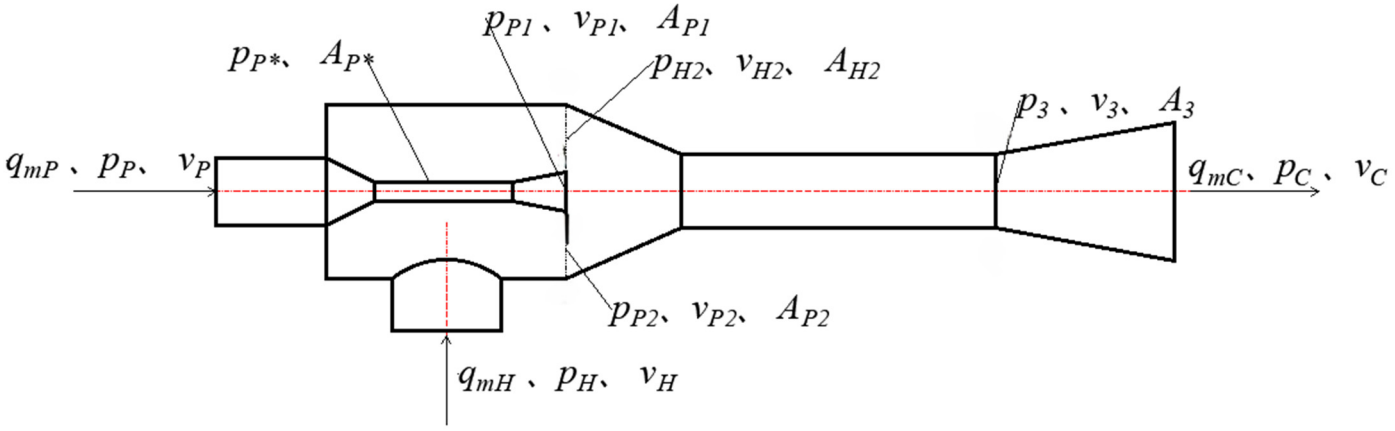


Figure 11. The schematic diagram of the vacuum generator cross-section and parameters.

The ejector coefficient formula can be derived through the analysis as follows:

$$\mu = \frac{K_1\lambda_{PH} - K_3\lambda_{C3}}{K_4\lambda_{C3} - K_2\lambda_{H2}} \frac{1}{\sqrt{\theta}} \tag{6}$$

where:

$$\begin{aligned} K_3 &= 1 + \varphi_3 \frac{p_C}{p_P} \frac{\Pi_{C3} - \frac{p_H}{p_C}\left\{\beta - 0.5(\beta-1)\Pi_{H2}\left[1+\left(\frac{p_C}{p_H}\right)\right]^{1-\alpha}\left(\frac{\Pi_{C3}}{\Pi_{H2}}\right)^{1-\alpha}\right\}}{\kappa\Pi_{P*}\lambda_{C3}q_{PH}\beta} \\ K_4 &= 1 + \varphi_4 \frac{p_C}{p_H} \frac{\Pi_{C3} - \Pi_{C2}\left\{\beta - 0.5(\beta-1)\left[1+\left(\frac{p_C}{p_H}\right)\right]^{1-\alpha}\left(\frac{\Pi_{C3}}{\Pi_{H2}}\right)^{1-\alpha}\right\}}{\kappa\Pi_{H*}\lambda_{C3}q_{H2}\beta} \end{aligned} \tag{7}$$

where φ—momentum transfer coefficient;

K—empirical constants ($K_1 = 0.834, K_2 = 0.812$);

λ—velocity coefficient;

θ—temperature ratio;

β—area ratio;

α—polytropic exponent.

Drawing on extensive experimental studies, Sokolov suggested that $K_1 = 0.834$, $K_2 = 0.812$, $\varphi_3 = 0.9$, $\varphi_4 = 0.925$.

When the inlet pressure reaches a certain value, the ejector velocity attains its limit; further increasing the pressure does not increase the flow rate but instead reduces efficiency. This is called the limiting state, and under this condition, the ejector coefficient is given by:

$$u_{MAX} = \frac{\mu\frac{p_H}{p_C}\frac{1}{q_{c3}} - \frac{p_H}{p_P}\frac{1}{q_{PH}}}{1 - \mu\frac{p_H}{p_C}\frac{1}{q_{c3}}} \frac{1}{\sqrt{\theta}} \tag{8}$$

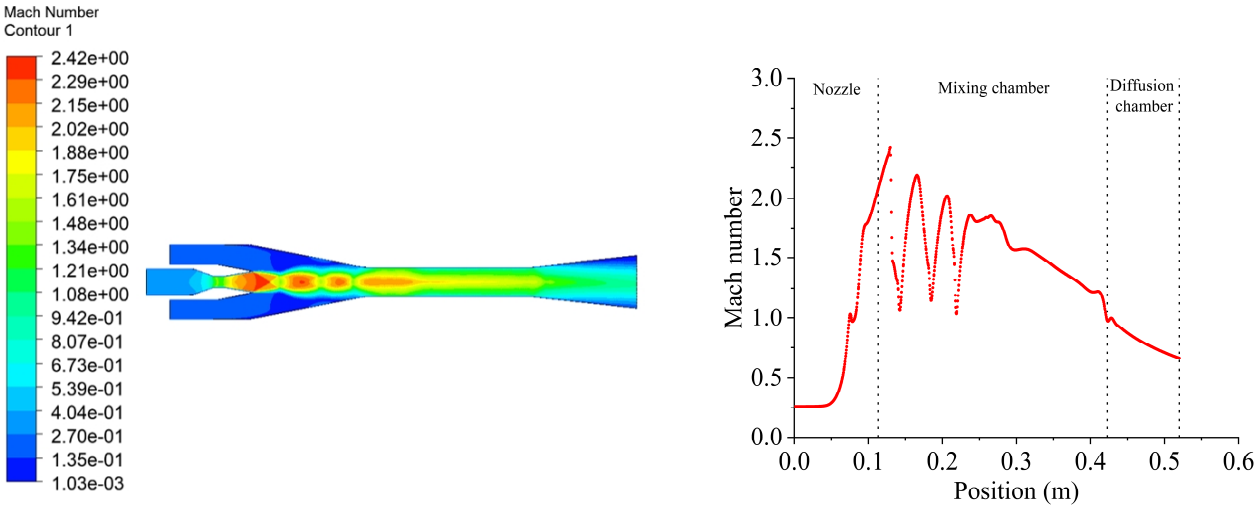
By using the ejector coefficient at the limiting state, combined with the formula, the optimal dimensions of the vacuum generator can be determined.

3.2.3. The Internal Flow Field Simulation and Analysis of the Vacuum Generator

The numerical simulations were conducted using ANSYS Fluent v221 2022 R1. Mesh Independence and Validation: Mesh independence was verified by comparing simulation results from three systematically refined meshes (0.8, 1.2, and 1.8 million hexahedral cells). The maximum deviation in predicted vacuum degree was below 2% between the medium and fine meshes, confirming that the 1.2-million-cell mesh provided a balance between accuracy and computational cost. Turbulence Modeling: The SST k–ω turbulence model was selected based on its validated performance in capturing shock waves and flow separation in supersonic ejectors, as demonstrated in prior studies [18,20]. This model combines the k–ω formulation near walls with the k–ε formulation in free-stream regions, providing accurate predictions for both boundary layer and compressible core flows. Numerical Uncertainty: Convergence was considered achieved when all residuals fell below 10^{-6} and monitored parameters (mass flow rate and pressure) varied by less than 0.1% over 1000 additional iterations. The discretization schemes were second-order upwind for momentum and energy, and first-order for turbulence quantities to ensure stability.

The computational domain was meshed with structured hexahedral elements (~1.2 million cells). The SST k-ω turbulence model was employed to capture the compressible flow behavior. The boundary conditions were set as follows: inlet pressure ranging from 100 to 600 kPa, atmospheric pressure at the outlet, and adiabatic no-slip walls. Convergence was achieved when all residuals fell below 10^{-5}. The geometric dimensions of the vacuum generator used in the simulation are as follows: the Laval nozzle throat diameter = 14.22 mm, outlet diameter = 27.45 mm, mixing chamber diameter = 36.74 mm, and diffuser outlet diameter = 59.65 mm.

The distribution of the Mach numbers inside the vacuum generator and its variation along the centerline are shown in Figure 12. From the Mach number distribution, the gas accelerates in the converging section, reaching sonic speed at the throat. In the diverging section, it further accelerates to supersonic speed before being discharged. Negative pressure is generated at the ejector outlet. Downstream in the mixing chamber, shock waves and expansion waves alternately reflect, causing fluctuations in the Mach numbers and pressure along the centerline.



(**a**) Mach number contour (**b**) Centerline Mach number variation curve

Figure 12. Mach number simulation results.

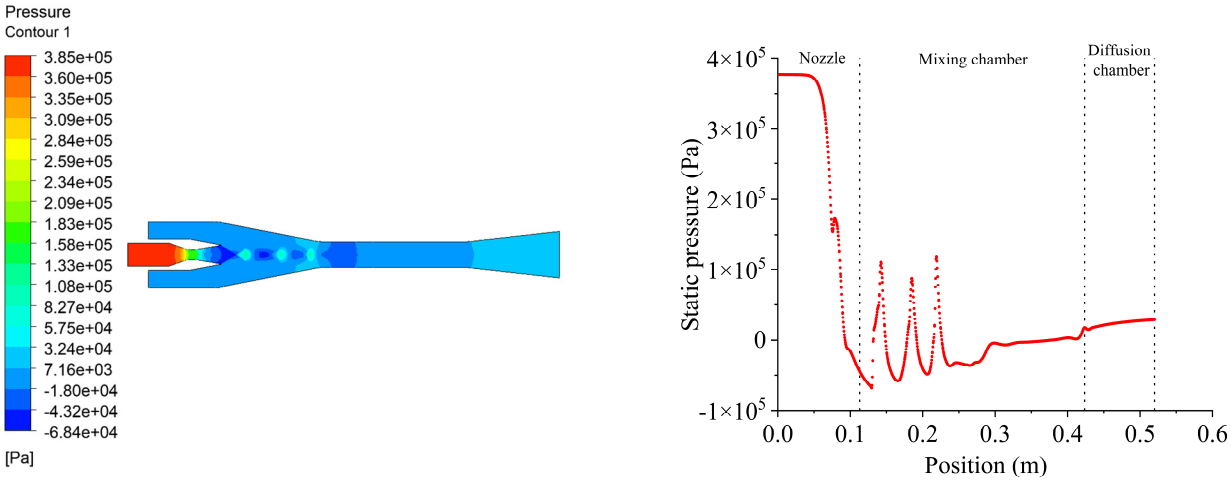
The internal pressure distribution in the vacuum generator and the pressure variation along the centerline are shown in Figure 13. The pressure simulation results indicate a significant pressure difference before and after the nozzle exit. The working fluid accelerates and drops in pressure at the throat, forming a low-pressure region between the mixing chamber inlet and the nozzle exit. The ejector fluid is drawn in by this pressure difference and mixes with the working fluid. During the mixing process, shock waves appear, causing complex pressure fluctuations. Due to the alternating effects of shock waves and expansion waves, the pressure along the centerline exhibits oscillations, characterized by an initial rise, then a fall, followed by another rise and fall, creating a distinct pressure fluctuation zone.

3.2.4. Analysis of the Effect of Inlet Pressure on Vacuum Degree

The variation in vacuum chamber pressure distribution in the vacuum generator under different inlet pressures is shown in Figures 14 and 15.

The vacuum degree reaches its maximum at an inlet pressure of 400 kPa. Beyond this point, the vacuum performance declines due to increased flow instability, shock wave formation, and energy losses within the Laval nozzle structure.

The simulation results indicate that as the inlet pressure increases, the vacuum degree first rises and then decreases. Between 100 and 400 kPa, the jetting effect strengthens, and the vacuum degree increases approximately linearly. Beyond 400 kPa, it tends to saturate, and above 500 kPa, the vacuum degree decreases, possibly due to instabilities such as shock waves or flow separation. This suggests that the vacuum performance is optimal within a reasonable pressure range, while excessively high pressure is detrimental.



(**a**) Static pressure contour plot (**b**) Static pressure variation curve along the centerline

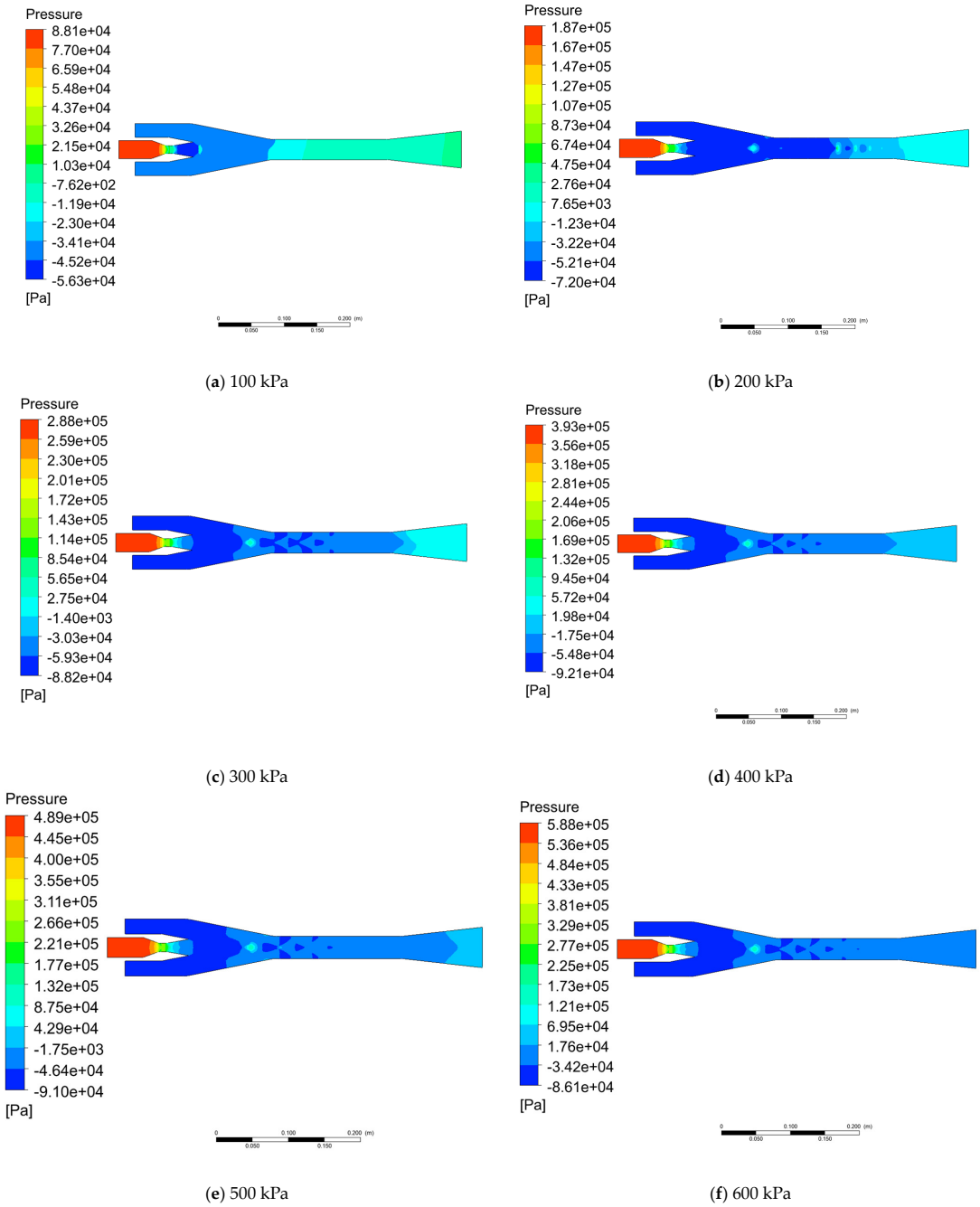
Figure 13. Pressure simulation results.

Physical Mechanism of Performance Degradation: The degradation of vacuum performance above 400 kPa is attributed to compressible flow effects within the Laval nozzle. CFD analysis reveals that at 500 kPa, a normal shock wave forms in the diverging section, causing abrupt pressure recovery and flow separation. This shock-induced dissipation reduces the effective pressure differential at the suction port, thereby decreasing both the vacuum degree and the mass flow rate. The dimensionless energy loss coefficient, calculated from the entropy generation rate, increases from 0.15 at 400 kPa to 0.23 at 600 kPa, indicating a 53% rise in irreversible losses. This phenomenon aligns with the critical pressure ratio theory for converging–diverging nozzles, where excessive inlet pressure drives the nozzle into an "over-expanded" condition with internal shock structures.

3.2.5. Analysis of the Effect of the Inlet Pressure on the Suction Flow Rate

Suction flow rate is a key indicator of vacuum generator performance and directly affects system transport efficiency. Although irregularities exist in the liquid phase during suction, the suction flow rate remains critical to system operation. To investigate the influence of inlet pressure, this study analyzes the variation of suction flow rate under different inlet pressures, as shown in Figure 16. The results indicate that although the initial flow fluctuates, it quickly stabilizes; curves above the zero line represent normal suction operation, while those below indicate backflow, signifying a loss of vacuum efficiency.

Further analysis based on Figure 17 shows that, while keeping other parameters constant, there exists an optimal inlet pressure: before this optimum point, the suction flow rate increases significantly with increasing inlet pressure. However, beyond this point, the suction flow rate gradually decreases.



(**a**) 100 kPa (**b**) 200 kPa

(**c**) 300 kPa (**d**) 400 kPa

(**e**) 500 kPa (**f**) 600 kPa

Figure 14. Vacuum chamber pressure under different inlet pressures.

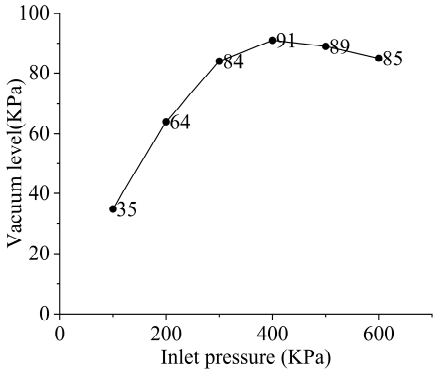


Figure 15. Vacuum degree variation curve with inlet pressure.

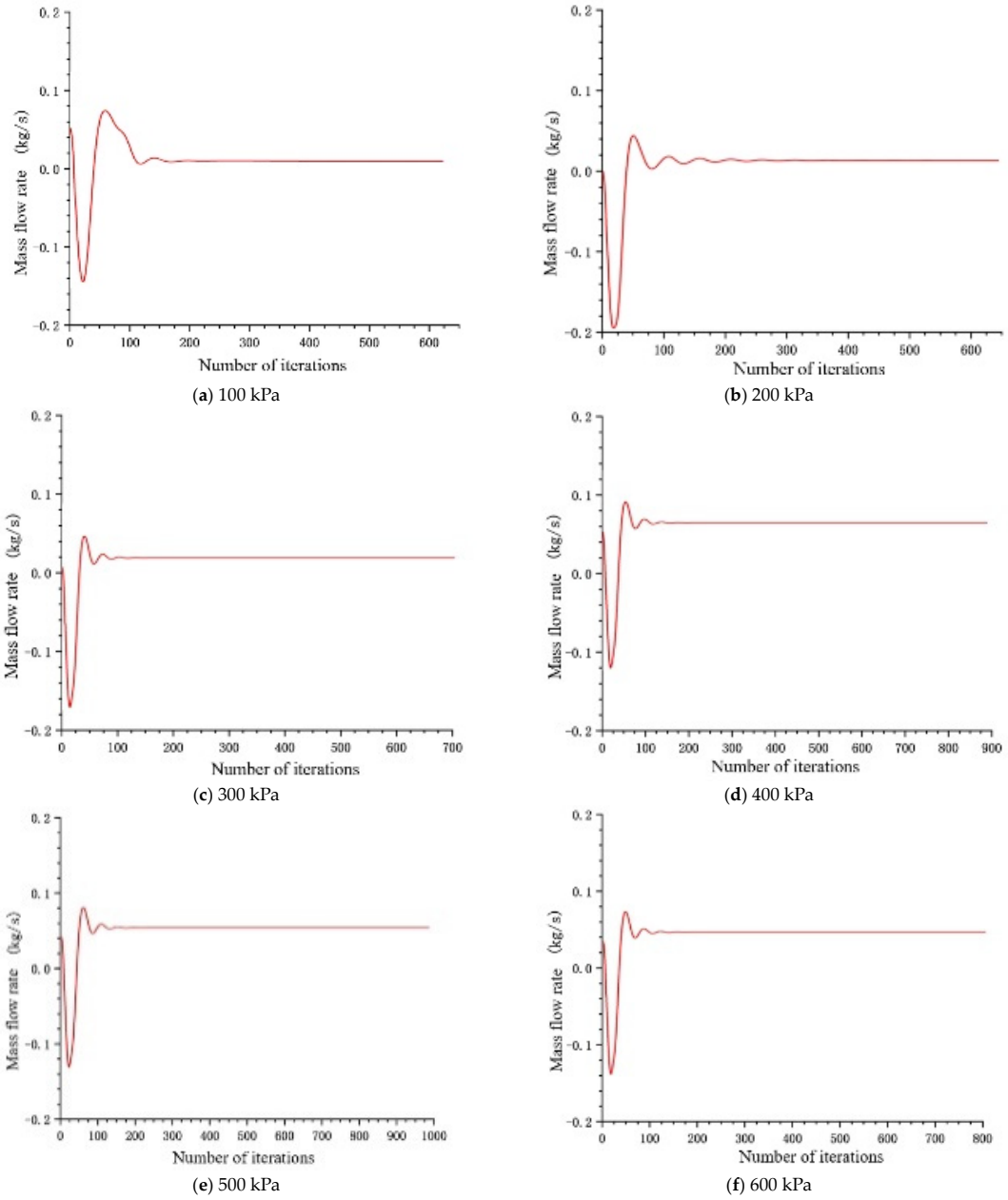


Figure 16. Simulation variation in suction flow rate under different inlet pressures.

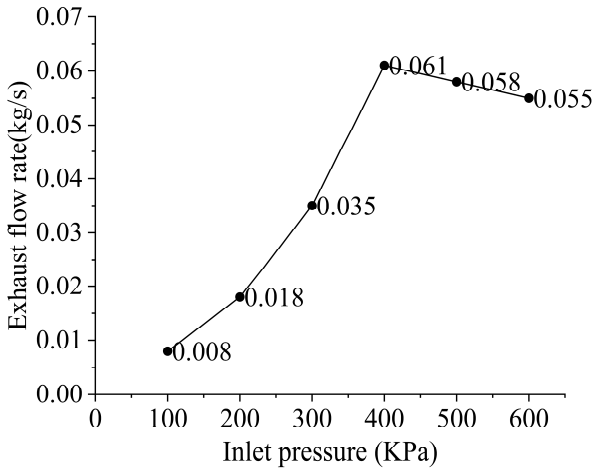


Figure 17. Mass flow rate variation curve with inlet pressure.

4. Prototype Testing of Negative-Pressure Suction Drill-Cuttings Reduction Equipment

Based on the preliminary design and simulation, a prototype of negative-pressure suction drilling cuttings reduction equipment is developed and experimentally tested in this section. The experiments focused on evaluating its operational performance, vacuum characteristics, and reduction efficiency under simulated working conditions. The dynamic monitoring of suction flow rate and vacuum degree was conducted to verify the accuracy of the simulation model and its engineering applicability.

4.1. Experimental Scheme and Components

4.1.1. Prototype Components of Negative-Pressure Suction Drill-Cuttings Reduction Equipment

The prototype of the negative-pressure suction drilling cuttings reduction equipment used the original design dimensions and was fabricated and assembled by a contracted manufacturer, as shown in Figure 18.

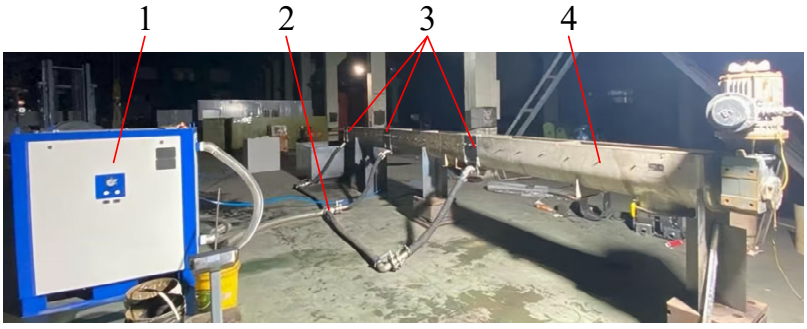


Figure 18. Experimental prototype. 1—vacuum transfer pump; 2—transfer pipeline; 3—negative-pressure suction short section; 4—screw conveyor.

The prototype was constructed based on the following key dimensions:

Negative-pressure suction section (filtration module): maximum mesh thickness = 11 mm; module structural thickness = 1.5 mm (stainless steel); positioning boss thickness = 0.5 mm; actual screen area ≈ 24,000 mm^2; and simplified simulation area = 50 mm^2 (1/480 scale).

Transfer pipeline: inner diameter = 65 mm; material = PTFE; bend curvature radius = 390–780 mm; and length = 5 m.

Screw conveyor: type = shaftless screw; fill rate controlled at 15–30%; and clearance between screw and screen ≈ 4 mm.

Vacuum generator: Laval nozzle throat diameter = 14.22 mm; outlet diameter = 27.45 mm; mixing chamber diameter = 36.74 mm; and diffuser outlet diameter = 59.65 mm.

Screen mesh: recommended mesh size = 100 mesh (aperture = 0.15 mm) and material = SS316 stainless steel.

Vacuum transfer pump: operating pressure range = 100–600 kPa; maximum vacuum achieved = 84.5 kPa (at 400 kPa inlet); and maximum suction flow rate = 0.0545 kg/s (at 400 kPa inlet).

4.1.2. The Design and Configuration of the Monitoring System

The pressure gauge used to monitor the operating pressure of the vacuum transfer pump is equipped on the prototype and does not require separate design or installation.

For measuring the suction flow rate, an insertion-type gas mass flow meter needs to be installed on the pipeline between the vacuum generator and the storage tank. The prototype has a reserved insertion port that remains sealed during normal operation and is opened for installing the flow meter during experiments.

To achieve real-time monitoring and data acquisition on drilling cuttings reduction, the system is centered around a PLC, combined with load cells and weight transmitters, to build a complete weight monitoring solution. The two sensors collect the weight of the solid and liquid phase containers. The signals are converted by the transmitters and input to the PLC for processing, then displayed and recorded in real time via upper-level software on a laptop.

Figure 19 shows the system wiring diagram, illustrating the connections between hardware signals and the power supply.

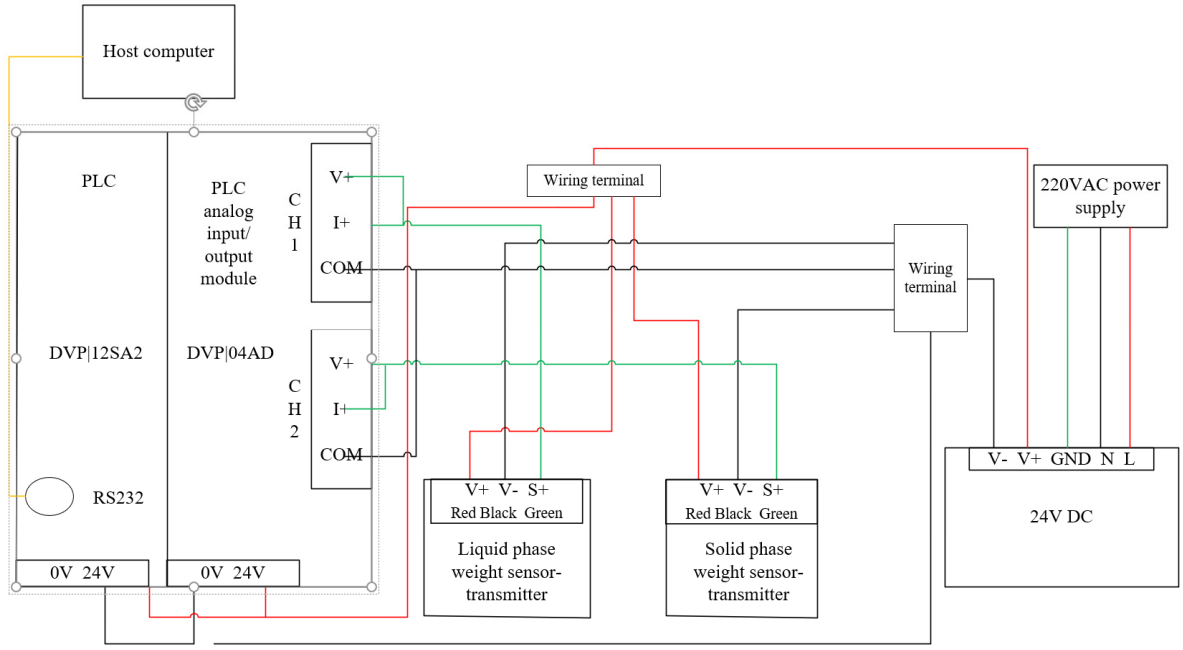


Figure 19. The wiring diagram of the weight monitoring system.

After completing the system design and wiring planning, the hardware assembly was carried out according to the drawings, as shown in Figure 20.

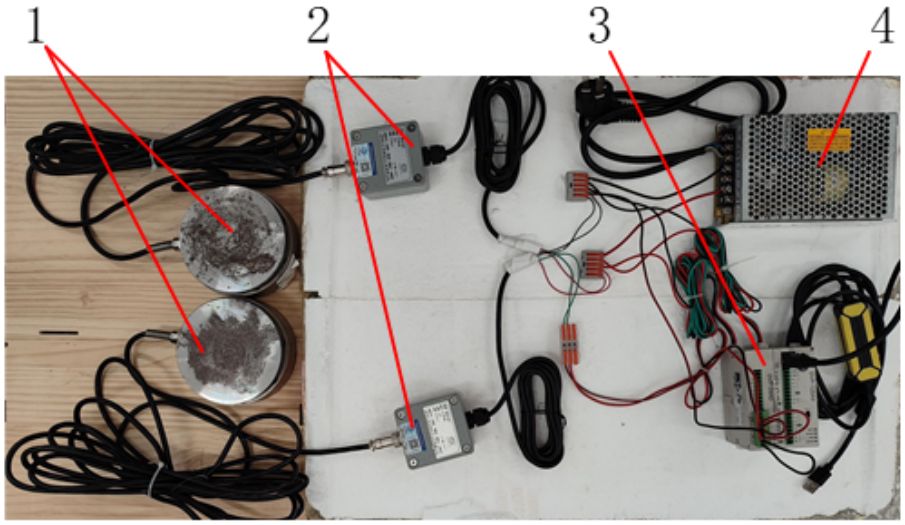


Figure 20. The physical hardware connection of the weight monitoring system. 1—solid and liquid phase weight sensor; 2—solid and liquid phase weight sensor transmitter; 3—PLC; 4—24 V power supply.

This experiment employed the Delta DIAView industrial SCADA software to design the human–machine interface (HMI), enabling real-time monitoring of weight variations in both liquid and solid phases.

By establishing communication with the PLC system, the sensor data is displayed in real-time on the operator interface, as illustrated in Figure 21.

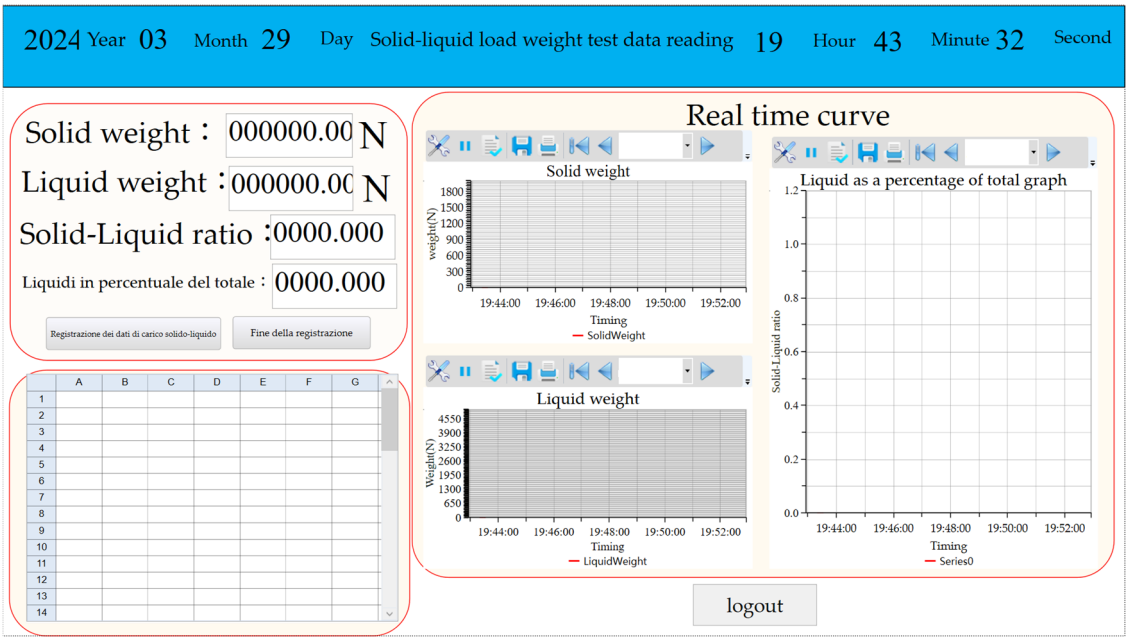


Figure 21. Upper computer interface for weight monitoring system.

4.2. Experimental Process and Data Analysis

4.2.1. Vacuum Conveying Pump Maximum Vacuum Level Test

After completing the assembly of the entire experimental prototype, the vacuum pressure test of the vacuum conveying pump was first conducted. All air inlets of the vacuum conveying pump were manually closed, leaving only the working air inlet of the vacuum generator, supplied with a constant-pressure gas stream and normal exhaust, to verify the simulation results from Section 3.2.4. The experiment utilized a factory air compressor with a pressure-regulating valve for gas supply. Under different inlet pressures, the pressure gauge readings were recorded once stabilized in the vacuum conveying pump's storage tank. Based on the simulation process in Section 3.2.4, the inlet pressure was set within a range of 100 kPa to 600 kPa, with tests conducted at 100 kPa intervals. Each pressure level was tested twice. When the pressure gauge in the storage tank stabilized, the recorded pressure values were converted into vacuum levels, as shown in Table 2.

Table 2. Experimental data on vacuum level under different inlet pressures.

Inlet Pressure (kPa)		**100**	**200**	**300**	**400**	**500**	**600**
Vacuum Level (kPa)	First Experiment	21	51	76	85	79	79
	Second Experiment	19	53	75	84	85	81
	Mean Value	20	52	75.5	84.5	82	80

As shown in Figure 22, the experimental mean values from Table 2 exhibit consistent trends with the simulation data in Section 3.2.4. Minor leakage occurred in the experiments,

whereas the simulation did not account for this factor, resulting in marginally lower maximum vacuum levels compared to ideal conditions.

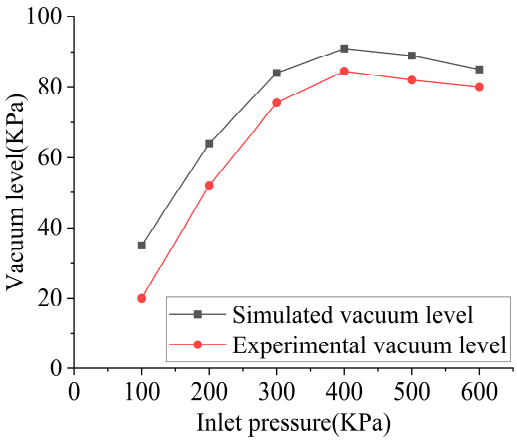


Figure 22. Comparative curves of vacuum level between experimental and simulation results under different inlet pressures.

4.2.2. Maximum Gas Extraction Rate Test of Vacuum Conveying Pump

Following the vacuum pressure tests, gas extraction rate measurements were conducted. A mass flow meter was installed on the vacuum conveying pump to directly sample ambient air without material loading. With the pump in extraction mode, stabilized flow readings were recorded after achieving steady-state conditions. The supply pressure, regulated by the factory air compressor through a pressure-reducing valve, was tested incrementally from 100 to 600 kPa at 100 kPa intervals. The stabilized flow rate data are presented in Table 3.

Table 3. Experimental data on gas extraction rate under different inlet pressures.

Inlet Pressure (kPa)		**100**	**200**	**300**	**400**	**500**	**600**
Gas Extraction Rate (kg/s)	First Experiment	0.006	0.015	0.028	0.056	0.053	0.050
	Second Experiment	0.005	0.013	0.026	0.053	0.051	0.052
	Mean Value	0.0055	0.014	0.027	0.0545	0.052	0.051

Figure 23 compares the experimental mean values from Table 3 with the simulation data in Section 3.2.5, showing generally consistent curve trends. The slightly higher simulated gas extraction rates are attributed to unaccounted minor leakage in actual experiments.

Each test condition was repeated three times, and the standard deviation of vacuum degree measurements was within ±1.5 kPa. Uncertainty analysis, considering instrument accuracy and environmental fluctuations, yielded a combined uncertainty of ±2.1% for reduction efficiency calculations.

The drilling cuttings used were sourced from the Bohai Sea Bozhong BZ29-6A33H platform, with a solid–liquid ratio of 1:4 representing typical water-based drilling returns in that region. While cuttings properties may vary across geological formations, the system's modular design—allowing adjustment to screen mesh (50–200 mesh), suction cycle timing (5–30 s), and conveyor speed (0.1–0.5 m/s)—provides adaptability to a range of operational conditions.

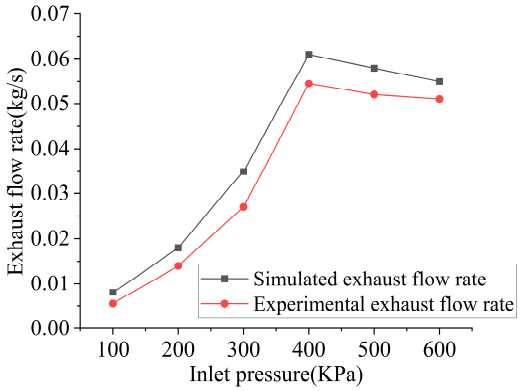


Figure 23. Comparative curves of gas extraction rate between experimental and simulation results under different inlet pressures.

4.2.3. Overall Equipment Reduction Efficiency Test

Following the completion of the previous experiments, the reduction efficiency test of the integrated system was conducted under actual operating conditions. With the inlet pressure set at 400 kPa, a solid–liquid mixture (ratio 1:4) of drilling cuttings sourced from a Bohai Sea offshore platform was fed into the screw conveyor where the key pre-experimental parameters of the mixture are detailed in Table 4. The fill rate was controlled at 15–30% by monitoring material height, covering three suction nodes with a total feed mass of 500 kg (~4900 N).

Table 4. Pre-experimental parameters of the solid–liquid mixture.

Total Mass of Material (N)	Solid-to-Liquid Ratio	Weight Percentage of Solid Phase (N)	Weight Percentage of Liquid Phase (N)
4900	1:4	980	3920

The test adopted a 10 s suction/5 s discharge cycle, with reduced conveyor speed during discharge, while maintaining a constant feed rate. Weight data from sensors beneath the container were transmitted to the HMI for real-time display and recording, enabling calculation of the suction flow rate and evaluation of solid–liquid separation efficiency. The weight monitoring results of the solid and liquid phases after the first test are presented in Table 5.

Table 5. Post-experimental weight monitoring parameters of solid and liquid phases (first test).

Effective Experimental Time (s)	Total Material Weight (N)	Weighed Solid Phase Mass (N)	Weighed Liquid Phase Mass (N)
420	4625	4204	421

To validate the initial results, a second experiment was conducted using the same procedure. The data are summarized in Table 6. Compared to the first test, material loss decreased, and the reduction efficiency improved to 9.86%. The outcomes of both tests exhibited consistent trends, which met expectations.

Table 6. Post-experimental weight monitoring parameters of solid and liquid phases (second test).

Effective Experimental Time (s)	Total Material Weight (N)	Weighed Solid Phase Mass (N)	Weighed Liquid Phase Mass (N)
435	4732	4249	483

5. Conclusions

This study systematically investigated the design, mechanism analysis, and experimental verification of a negative-pressure suction-based cuttings reduction device, aiming to enhance the treatment capacity and operational efficiency of the solid control system during offshore drilling. The main research conclusions are as follows:

(1). Overall Design: A novel negative-pressure suction cuttings reduction system was designed and fabricated, integrating a vacuum generator with a screw conveyor for enhanced solid–liquid separation.

(2). Vacuum Generation Mechanism: The vacuum generation mechanism was analyzed theoretically and validated through CFD simulations. The optimal inlet pressure was identified as 400 kPa, yielding a maximum vacuum degree of 84.5 kPa and a suction flow rate of 0.0545 kg/s. The vacuum degree reached its maximum at an inlet pressure of 400 kPa. Beyond this point, the vacuum performance declined due to increased flow instability, shock wave formation, and energy losses within the Laval nozzle structure.

(3.) Experimental Validation: A complete prototype system and monitoring platform were built to conduct experiments on maximum vacuum level, maximum suction flow rate, and overall reduction efficiency. The experimental results showed good agreement with simulation predictions. The measured reduction efficiency reached 9.225–9.86%, more than double the target value set by the project. Compared with the vacuum performance reported by Wang Zhongyi et al. [21] for similar ejector structures, the vacuum degree achieved in this study (84.5 kPa at 400 kPa inlet pressure) represents a 12% improvement, likely due to the optimized Laval nozzle geometry and enhanced mixing chamber design.

(4.) This study provides a new theoretical framework and engineering foundation for the systematic application of vacuum negative-pressure technology in solids control during oil and gas drilling. Furthermore, after passing prototype testing, the developed equipment was successfully applied in offshore field trials on platforms Haiyang Shiyou 947M23 and Bo zhong BZ29-6A33H, achieving favorable results and meeting the specified performance indicators.

While this study demonstrates technical feasibility under controlled conditions, several practical limitations warrant consideration for industrial deployment:

(1). Energy Efficiency: The current system consumes approximately 15 kW at optimal operation (400 kPa inlet). For continuous 24/7 platform operation, energy optimization through variable-frequency drive control of the air compressor and waste heat recovery from compressed air should be investigated.

(2). Long-term Durability: The filtration module, particularly the 100-mesh screen, showed visible wear after 50 h of continuous testing with abrasive cuttings. Material upgrades (e.g., tungsten carbide coating) or modular replacement designs are needed for extended service life.

(3). Scalability to Platform Scale: Scaling from a laboratory prototype (500 kg/h) to full platform capacity (5–10 t/h) requires careful consideration of footprint constraints, integration with existing solids control equipment, and maintenance accessibility. A modular, containerized design approach is recommended.

(4). Adaptability to Variable Feedstock: The system performance was validated with cuttings from a specific geological formation. Additional testing with cuttings of varying clay content, oil contamination, and particle size distribution is necessary to define operational envelopes.

These limitations do not negate the system's potential but highlight areas for further development prior to widespread adoption.

6. Future Work Recommendations

(1). Investigate the effects of varying drill-cuttings properties (e.g., particle size distribution and viscosity) on separation efficiency.
(2). Optimize the multi-stage suction layout and cycle timing to further improve energy efficiency.
(3). Develop a predictive maintenance model based on real-time sensor data to extend equipment service life in harsh offshore environments.

Author Contributions: Conceptualization, X.W.; Methodology, X.W.; Software, X.W.; Validation, X.W., Z.W., and H.M.; Investigation, Z.W.; Resources, B.Z. and H.M.; Data curation, H.M.; Writing—original draft, X.W.; Writing—review and editing, X.W.; Supervision, B.Z., Z.W., and H.M.; Project administration, B.Z., Z.W., and H.M.; Funding acquisition, B.Z. All authors have read and agreed to the published version of the manuscript.

Funding: This research was supported by the National Natural Science Foundation of China (grant number 51879063).

Data Availability Statement: The data presented in this study are available on request from the corresponding author due to the confidentiality requirements of the research project and the relevant confidentiality regulations of the project's commissioning company. The research data involves confidential information of the project, which cannot be disclosed publicly in accordance with the above-mentioned confidentiality provisions.

Conflicts of Interest: The authors declare no conflicts of interest.

References

1. Yang, J.; Li, L.; Song, Y.; Tong, G.; Zhang, M.; Zhang, H. Current status and prospects of offshore oil and gas drilling technology in China. *Acta Pet. Sin.* **2023**, *44*, 2308–2318. [CrossRef]
2. Sui, D.; Zhan, M.; Sui, D.; Zhao, F. Regulations and methods for disposal of waste drilling fluid. *IOP Conf. Ser. Earth Environ. Sci.* **2021**, *631*, 012045. [CrossRef]
3. Peng, B.; Liu, W.; Gao, J.; Yu, F.; Li, X. Research progress on harmless treatment technology of waste drilling fluids. *Geol. Equip.* **2024**, *25*, 39–44. Available online: https://kns.cnki.net/kcms2/article/abstract?v=cDHjH8kzCu2OQNSxn6hi9MxvPmMDD5nBAwvXIjptCT3PeNRgwG1nJj652GUZmxh6fR4ZpBCPLtDAfa2XOr_vEqOIVVnOCkUpUDvaNKzqSrVVlsG7vqu4THAl8NOl7k2jLSY2iXXFZv184swZLxQCCkBwdpJTNK79VxHg2oUJhwqiyGwumEN0PQ==&uniplatform=NZKPT&language=CHS (accessed on 4 February 2026).
4. Zhang, Y.; Yue, M.; Chen, Y.; Liu, H.; Yang, X. Applicability analysis of drilling waste disposal technology in Bohai oilfield. *Oil Gas Field Environ. Prot.* **2019**, *29*, 26–28, 36. [CrossRef]
5. Njuguna, J.; Siddique, S.; Bakah Kwroffie, L.; Piromrat, S.; Addae-Afoakwa, K.; Ekeh-Adegbotolu, U.; Oluyemi, G.; Yates, K.; Mishra, A.K.; Moller, L. The fate of waste drilling fluids from oil & gas industry activities in the exploration and production operations. *Waste Manag.* **2022**, *139*, 362–380. [CrossRef] [PubMed]
6. Yue, M.; Liu, Y.; Li, Z.; Lin, J.; Liu, H. Discussion on cuttings reduction treatment technology of water-based drilling fluids. *Unconv. Oil Gas* **2021**, *8*, 39. [CrossRef]
7. Liu, J.; Li, G.; Xia, Y. Technical Progress on Environmental-Friendly, High-Performance Water-Based Drilling Fluids. *Environ. Earth Sci. Res. J.* **2020**, *7*, 121–126. [CrossRef]
8. Wang, Z. Current situation and development suggestions for drilling fluid technologies in China. *Pet. Drill. Tech.* **2023**, *51*, 114–123. [CrossRef]
9. Luo, P.; Yan, C.; Chen, Z.; Zhao, Z.; Guan, H. Current status and development trends of drilling fluid solids control equipment research. *Pet. Ind. Technol. Superv.* **2024**, *40*, 67–71.
10. Wang, W. Optimization of solid phase control technology in Jidong oilfield. *Drill. Fluid Complet. Fluid* **2018**, *35*, 47–52. [CrossRef]

11. Xie, J.; Ma, Z.; Zhang, Y.; Shao, T.; Meng, D. Study on the migration law of solid particles on spiral belt negative-pressure vibrating screen. *Pet. Field Mach.* **2020**, *49*, 15–21. Available online: https://kns.cnki.net/kcms2/article/abstract?v=cDHjH8kzCu2o-1NSEDjy3x2PgQAkbZ_Qt62P_9MM4Ue6M6Y4H97W1m8VghKb26Mx6r9QSBBRSdSsCBwMT4sPpESmf2S_tTqE_iOsAlWwZpAkBXGnv-AVhHu6YTSARMgsFKWYgUhFzbUhjS4NzXFN677nN_PgR7lbgbL12tQnzZy4q9uJnz-ZuQ==&uniplatform=NZKPT&language=CHS (accessed on 4 February 2026).
12. Schlumberger. Screen Pulse Fluid and Cuttings Separator [Product Page]. 1 May 2015. Available online: https://www.slb.com/products-and-services/innovating-in-oil-and-gas/well-construction/drilling-fluids/solids-control/shakers/screen-pulse-cuttings-separator (accessed on 1 July 2023).
13. Zhou, S.; Li, X.; Lyu, Z.; Cui, Y. Dynamic characteristic analysis of negative pressure drilling vibrating screen. *Mech. Des. Manuf.* **2018**, *10*, 43–46. [CrossRef]
14. Ma, W.; Wu, J.; Xu, Z.; Hu, X.; Mou, C.; Liu, S.; Zhang, H.; Zeng, Q.; Yang, Y. A Method for Screening and Drying Treatment of Drilling Fluid Mud and a Drilling Fluid Mud Screening Device. Chinese Patent No. CN106939773B, 15 March 2019. Available online: https://patents.google.com/patent/CN106939773B/en (accessed on 4 February 2026).
15. Wu, J.; Ma, W.; Lei, X.; Chai, Z.; Hou, Z.; Liu, S.; Mei, X.; Chen, S.; Wang, G. A Vibrating Screen for Drilling Fluid Mud. Chinese Patent No. CN106955840B, 3 February 2023. Available online: https://patents.google.com/patent/CN106955840B/en (accessed on 4 February 2026).
16. Ma, S.; Wang, X. Numerical simulation and optimization design of key structural parameters of ejector. *Mech. Eng. Autom.* **2024**, *4*, 55–57. [CrossRef]
17. Sokolov, E.Y.; Zinger, N.M. *Ejectors*; Huang, Q., Translator; Science Press: Beijing, China, 1977. Original work published 1970.
18. Croquer, S.; Poncet, S.; Aidoun, Z. Turbulence modeling of a single-phase R134a supersonic ejector. Part 1: Numerical benchmark. *Int. J. Refrig.* **2016**, *61*, 140–152. [CrossRef]
19. Li, T. Structural Optimization and Study of New Nozzles for Ejector Vacuum Pumps. Master's Thesis, China University of Petroleum (East China), Qingdao, China, 2016. Available online: https://kns.cnki.net/kcms2/article/abstract?v=cDHjH8kzCu151l4sIVXTWtVn5_9nKL67g1y-hbmHpNwh8SQ-qOHPfN5VqDhze75qtAyj_gMtvm_Q-c26aO25T63pg833PqVFiho_mVVDSI8zIrMzhRddo4VGeTiRuZtbqF2t64CeDbM-pNu8xXiNfPkSbZBie_5iFoV8pmZKcUt2uUXBj3EcX80-QiPepgSu&uniplatform=NZKPT&language=CHS (accessed on 4 February 2026).
20. Dong, J.; Hu, Q.; Yu, M.; Han, Z.; Cui, W.; Liang, D.; Ma, H.; Pan, X. Numerical investigation on the influence of mixing chamber length on steam ejector performance. *Appl. Therm. Eng.* **2020**, *174*, 115204. [CrossRef]
21. Wang, Z.; Jiang, P.; Li, Z.; Li, Y.; Guo, X. Analysis of vacuum level characteristics in vacuum generators for negative pressure conveyance. *Mach. Manuf. Autom.* **2021**, *50*, 215–218. [CrossRef]
22. Zhao, Z.; Wang, Z.; Xiong, W.; Wang, H. Energy efficiency analysis of pneumatic vacuum generators based on the exergy field method. In *Proceedings of the 2023 9th International Conference on Fluid Power and Mechatronics (FPM)*; IEEE: New York, NY, USA, 2023; pp. 1–10. [CrossRef]
23. Zhang, B.; Lu, H.; Yang, J.; Sun, P.; Deng, L. Numerical study of the coupling collection flow field and collecting mechanism of swirling flow and negative pressure suction flow in deep sea mining. *Ocean Eng.* **2024**, *309*, 118373. [CrossRef]
24. Liu, Y.; Xu, F. *Hydraulic and Pneumatic Transmission*, 4th ed.; China Machine Press: Beijing, China, 2018.

Disclaimer/Publisher's Note: The statements, opinions and data contained in all publications are solely those of the individual author(s) and contributor(s) and not of MDPI and/or the editor(s). MDPI and/or the editor(s) disclaim responsibility for any injury to people or property resulting from any ideas, methods, instructions or products referred to in the content.